

Power deposition profiles during  
Lower Hybrid Heating of Tokamak plasmas.

M. Brambilla

IPP 4/200

Mai 1981



**MAX-PLANCK-INSTITUT FÜR PLASMAPHYSIK**

**8046 GARCHING BEI MÜNCHEN**



**MAX-PLANCK-INSTITUT FÜR PLASMAPHYSIK**  
**GARCHING BEI MÜNCHEN**

Power deposition profiles during  
Lower Hybrid Heating of Tokamak plasmas.

M. Brambilla

IPP 4/200

Mai 1981

*Die nachstehende Arbeit wurde im Rahmen des Vertrages zwischen dem  
Max-Planck-Institut für Plasmaphysik und der Europäischen Atomgemeinschaft über die  
Zusammenarbeit auf dem Gebiete der Plasmaphysik durchgeführt.*

Abstract

A ray-tracing numerical code has been adapted to evaluate the power deposition profiles during Lower Hybrid heating of Tokamak plasmas. In the first part of this report we briefly introduce the physical model of LH heating which is used, and the equations solved by the code. We then describe the approximations which allow a rapid evaluation of the absorption by ions and by electrons as a function of radius, from the results of the ray-tracing subroutine. These profiles are ready for use as heat sources in a radial transport-code simulating the Tokamak discharge. Finally, we present a set of examples relevant for the LH heating experiment planned on the ASDEX Tokamak.

## 1. Introduction

Propagation and absorption of Lower Hybrid waves are most naturally discussed in terms of  $k_{\parallel}$  and  $k_{\perp}$ , the components of the wavevector parallel and perpendicular to the static magnetic field  $\vec{B}_0$ , respectively. As a first approximation, it is assumed that  $k_{\parallel}$  (rather, a spectrum of  $k_{\parallel}$ ) is imposed by the periodicity of the antenna along  $\vec{B}_0$ , and the local dispersion relation is used to obtain  $k_{\perp}$  as a function of the position in the plasma. A very useful rapid insight into the conditions for accessibility of the plasma core to the waves and for their absorption there can be gained in this way.

In a Tokamak, however,  $k_{\parallel}$  is not strictly constant, essentially because the surfaces of constant density and temperature (the magnetic surfaces) are not at the same time surfaces of constant  $|\vec{B}_0|$ . In terms of  $k_{\parallel}$  and  $k_{\perp}$ , the conditions for accessibility or absorption are locally the same as in the one dimensional case. To know  $k_{\parallel}$  and  $k_{\perp}$  at each point in the plasma, however, one has to use ray tracing.

This technique has been used by several authors /1/-/8/ and has given quantitative results on accessibility as well as insight into the qualitative features of LH wave propagation in toroidal geometry. For the planning and interpretation of LH heating experiments, however, it is also of importance to be able to calculate the radial distribution of absorption by ions and electrons.

In this report we describe the use of a numerical ray-tracing subroutine developed by A. Cardinali and M. Brambilla /9/ for the evaluation of power deposition profiles during Lower Hybrid Resonance heating of tokamak plasmas. As a preliminary, we discuss briefly the dispersion relation assumed, and the set of ray equations which are integrated by the code. We then recall the conditions for absorption of LH waves by the ions or the electrons, and we describe the method and the approximations made to obtain the radial power deposition profile, given the power spectrum of the antenna and the density and temperature profiles in the plasma. Finally, some example relevant for the planned LHR heating experiment on the ASDEX tokamak are presented.

## 2. The dispersion relation

Lower Hybrid Resonance heating is based on the excitation and absorption of waves belonging to the slow branch of the cold plasma dispersion relation in the GHz frequency range.



A simple, yet accurate dispersion relation for waves in this frequency range can be obtained by assuming that the ions are essentially unmagnetized ( $\omega \ll \Omega_{ce}$ ), and including only the lowest order thermal corrections /10/. Under these assumptions, the dispersion relation of LH waves depends on density, temperature, magnetic field, and plasma composition only through the following parameters:

$$\sum_j \frac{\omega_{pj}^2}{\omega^2} = X \eta \quad (1)$$

$$X = \frac{\bar{\omega}_{pH}^2}{\omega^2} = 4.41 \frac{10^{-14} n_e}{f^2} \quad \eta = \sum_j \frac{Z_j^2 \alpha_j}{A_j}$$

$$\sum_j \frac{\omega_{pj}^2}{\omega^2} \frac{U_{Tj}^2}{C^2} = 4.264 \cdot 10^{-6} T_i \cdot X \xi \quad (2)$$

$$\xi = \sum_j \frac{Z_j^2 \alpha_j}{A_j^2}$$

$$y^2 = \frac{\omega^2}{\Omega_{cH} \Omega_{ce}} = 9.368 \frac{f^2}{B^2} \quad (3)$$

Here  $f$  is the applied frequency in GHz,  $n_e$  the electron density per  $\text{cm}^3$ ,  $B$  the static magnetic field in Tesla, and  $T_e$ ,  $T_i$  the temperatures in keV.  $\alpha_H$ ,  $\alpha_D$ ,  $\alpha_T$ ,  $\alpha_{Zi}$  are the numerical concentrations,

$$\alpha_j = \frac{n_j}{n_e} \quad (4)$$

while  $\bar{\omega}_{pH}$  is the ion plasma frequency of a pure hydrogen plasma having electron density  $n_e$ . Note that both  $X$  and  $y^2$  are of order unity in the centre of the plasma.

With these notations, the dispersion relation of LH waves can be written as a cubic in the perpendicular index squared,

$$H(\omega, \vec{k}) = -\alpha n_{\perp}^6 + A n_{\perp}^4 - B n_{\perp}^2 + C \quad (5)$$

where  $n_{\perp}^2 = k_{\perp}^2 c^2 / \omega^2$ ,  $n_{\parallel}^2 = k_{\parallel}^2 c^2 / \omega^2$ ,

$$\alpha = 4.6 \cdot 10^{-6} X (\xi T_i + y^4 T_e) \quad (6)$$

$$A = 1 + X (y^2 - \eta)$$

$$B = H X (n_{\parallel}^2 - 1 - X (2y^2 - \eta))$$

$$C = H^2 X^3 y^2 - H X (n_{\parallel}^2 - 1)$$

and  $M = M_H/m_e = 1836.2$  is the proton to electron mass ratio.

Eq. (5) describes three waves, namely the fast cold-plasma wave  $n_{\perp}^2 \approx C/B$ , the slow plasma wave  $n_{\perp}^2 \approx B/A$ , and the electrostatic L.H. wave  $n_{\perp}^2 \approx A/\alpha$ . Since the coefficients of Eq. (5) are ordered as successive powers of  $M \gg 1$ , this approximate factorization breaks down only in the vicinity of double roots, of which two kinds exist:

a) Confluence between the slow and fast wave,

$$n_{//} = n_{//CONF} \approx \sqrt{Xy^2} + \sqrt{1 + X(y^2 - \eta)} \quad (7)$$

which affects the accessibility of the plasma centre for slow waves with  $n_{//}$  below a certain value  $/11/$ ; and

b) Confluence between the slow and the electrostatic waves, also known as Linear Turning Point  $/12/$ :

$$n_{//} = n_{//LTP} \approx \left[ 1 + X(y^2 - \eta) + \frac{(1 + X(y^2 - \eta))^2}{2.35 \cdot 10^{-2} X^2 (\xi T_i + y^4 T_e)} \right]^{1/2} \quad (8)$$

which determines the region of effective ion heating.

### 3. The ray equations

A comprehensive discussion of the Eikonal approximation for LH waves will be published elsewhere  $/13/$ . Here it will be sufficient to recall that due to the slow wave nature of the coupling structure, ray tracing must be implemented separately for each partial wave with given toroidal number  $n_{\varphi}$ . The Eikonal Ansatz then reads

$$\begin{aligned} \vec{E} &= \vec{E}_{n_{\varphi}}(r, \vartheta) \exp i(n_{\varphi} \varphi + S_{n_{\varphi}}(r, \vartheta) - \omega t) \\ \vec{k} &= \text{grad}(n_{\varphi} \varphi + S_{n_{\varphi}}(r, \vartheta)) \end{aligned} \quad (9)$$

or explicitly, in toroidal coordinates  $r, \vartheta, \varphi$

$$\begin{aligned} k_{\perp}^2 &= k_r^2 + k_{\chi}^2 \\ k_{\chi} &= \frac{m_{\theta}}{r} \cos(\vartheta) - \frac{n_{\varphi}}{R h_s} \sin(\vartheta) \\ k_{//} &= \frac{m_{\theta}}{r} \sin(\vartheta) + \frac{n_{\varphi}}{R h_s} \cos(\vartheta) \end{aligned} \quad (10)$$

Here

$$\tan \Theta = \frac{B_\theta}{B_\phi} = \frac{z}{Rq(z)} \quad (11)$$

$$h_s = 1 + \frac{z}{R} \cos \vartheta \quad (12)$$

and  $(k_r, m_\theta, n_\phi)$  are the covariant components of  $\vec{k}$ . We are of course assuming wavelength so short that quantization of  $m_\theta$  can be disregarded.

The ray trajectories and  $\vec{k}$  along the rays can then be computed from the ray equations

$$\frac{dz}{d\tau} = \frac{\partial H}{\partial k_z} \quad \frac{d\vartheta}{d\tau} = \frac{\partial H}{\partial m_\theta} \quad (13)$$

$$\frac{dk_z}{d\tau} = -\frac{\partial H}{\partial z} \quad \frac{dm_\theta}{d\tau} = -\frac{\partial H}{\partial \theta} \quad (14)$$

(the  $\phi$  coordinate can be ignored in this context). Here  $\tau$  is an appropriate parameter along the ray without physical meaning. In the applications it is more convenient to use  $S_{n_F}$  as independent variable, eliminating  $\tau$  through

$$\frac{dS_{n_F}}{d\tau} = -\left(k_z \frac{\partial H}{\partial z} + m_\theta \frac{\partial H}{\partial \theta}\right) \quad (15).$$

The r.h.s. of the ray equations (13)-(14) are easily evaluated using (10) and the familiar rules of implicit derivation:

$$\begin{aligned} \frac{\partial H}{\partial m_\theta} &= \frac{2}{z} \left( k_\chi \cos \Theta \frac{\partial H}{\partial k_\perp^2} + k_\parallel \sin \Theta \frac{\partial H}{\partial k_\parallel^2} \right) \\ \frac{\partial H}{\partial n_\phi} &= \frac{2}{Rh_s} \left( -k_\chi \sin \Theta \frac{\partial H}{\partial k_\perp^2} + k_\parallel \cos \Theta \frac{\partial H}{\partial k_\parallel^2} \right) \\ \frac{\partial H}{\partial z} &= \sum_i e \left( \frac{1}{T} \frac{dT}{dz} \right) T \frac{\partial H}{\partial T} + \frac{1}{n} \frac{dn}{dz} \chi \frac{\partial H}{\partial \chi} - \frac{m_\theta}{z} \frac{\partial H}{\partial m_\theta} \\ &\quad + \frac{\cos \vartheta}{Rh_s} \left( 2y^2 \frac{\partial H}{\partial y^2} - n_\phi \frac{\partial H}{\partial n_\phi} \right) + \\ &\quad - 2k_\chi k_\parallel \left( \frac{\partial H}{\partial k_\perp^2} - \frac{\partial H}{\partial k_\parallel^2} \right) \frac{d\Theta}{dz} \\ \frac{\partial H}{\partial \theta} &= 2 \frac{z \sin \vartheta}{Rh_s} \left( -y^2 \frac{\partial H}{\partial y^2} + n_\phi \frac{\partial H}{\partial n_\phi} \right) \end{aligned} \quad (16)$$



As initial conditions for the integration of the system (13)-(14), it is assumed that the initial wavefront is a strip of magnetic surface  $r = r_0$  in front of the antenna, so that  $m_\theta = 0$  there. Given  $n_\phi$ , the dispersion relation can be used to obtain the value of  $k_r$  on the initial wavefront. The constancy of  $H = 0$  (to a relative precision  $\sim 10^{-6}$ ) is used as an independent check of the integration accuracy.

#### 4. Absorption of LH waves

Absorption of LH waves by the ions occurs through a stochastic process, essentially equivalent to ion Landau damping by unmagnetized ions /14/. This ion-wave interaction requires a sufficient number of ions satisfying the Cerenkoff resonance condition  $\omega/k_{\perp}v_{\perp} \approx 1$ ; hence absorption by the ions will be localized where

$$\frac{\omega}{k_{\perp}v_{thi}} \approx q_i \quad (17)$$

where  $q_i$  is a number of the order of a few units. If enough collisions are present to maintain the distribution function maxwellian in spite of the absorption,  $q_i \approx 4$ ; it can be reduced somewhat ( $q_i \gtrsim 2.5-3$ ) if nonlinear saturation is important. It is well known that condition (17), requiring quite large values of  $n_{\perp}^2$ , can be satisfied only in the vicinity of the Linear Turning point; this in turn implies that ion heating is restricted to an appropriate range of densities such that the Linear Turning Point is present in the plasma centre for the values of  $k_{\parallel}$  excited by the antenna. The only exception occurs in the presence of a minority of light ions (e.g.  $H^+$  in a  $D^+$  plasma) with concentration sufficient to efficiently absorb the wave, but low enough not to affect appreciably the L.T.P. location /10/.

Electrons can absorb LH waves by parallel Landau damping whenever

$$\frac{\omega}{k_{\parallel}v_{the}} \approx q_e \quad (18)$$

where  $q_e$  has the same meaning and numerical values as  $q_i$  in eq. (17) above. To the extent that  $k_{\parallel}$  is little affected by the plasma parameters ( $k_{\parallel}$  being a constant in the slab model) electron heating depends only on the electron temperature profile and is independent from the plasma density /15/.

Power depletion by other processes, such as parametric decay, has not been included in the present model.

## 5. Evaluation of power deposition profiles

Strictly speaking, Eqs. (13)-(14) do not suffice to evaluate power deposition profiles: they should be supplemented by an equation for the slowly varying amplitude of the wave,  $|\vec{E}_{n\varphi}(\tau, \vartheta)|$ , along the ray. Such an equation is quite complicated: it must take into account, in addition to the local absorption, also the local polarization of the fields, and the geometry of the ray pencil (curvature, focussing, etc.).

We will present elsewhere /3/ the appropriate equation, and examples obtained by integrating it. Here we want to point out that the exact approach is rather heavy to use in conjunction with a transport code, and the accuracy it offers is rather illusory in view of the relative coarseness of the radial mesh of transport codes.

As a ray with given  $n_{\varphi}$  propagates inwardly, its absorption is found to be negligible up to a certain point, where condition (17) or (18) begin to be satisfied. From then on absorption proceeds quite rapidly, due to the very short wavelengths, and to the exponential increase of the relative damping per wavelength as the ratio of the wave phase velocity to the particle thermal velocity decreases. Typically, absorption is complete in a radial distance comparable or smaller than the radial distance  $\Delta r$  between adjacent mesh points.

This suggests to simply stop ray tracing at the point where either condition (17) or condition (18) are satisfied, and to assume that the power radiated by the antenna on the corresponding partial wave is absorbed there. This approach is much faster, yet perfectly adequate. The exact energy transport equation is only used to "calibrate" Eqs. (17) and (18), i.e. to choose the most appropriate values for  $q_i$  and  $q_e$ . If linear Landau damping is assumed, these values turn out to be

$$q_i \approx q_e \approx 3.9 \quad (19)$$

In practice, the evaluation of the power deposition profile proceeds as follows. The power spectrum  $P(n_{\parallel a})$  radiated by the antenna is first computed using a previously developed code /16/. Using the density temperature and poloidal field profiles provided by the transport code, ray tracing is implemented for a sufficiently large number of values of  $n_{\parallel \bar{\alpha}}$  (here  $n_{\parallel \bar{\alpha}}$  means the initial value of  $n_{\parallel}$ , just in front of the antenna);

typically, 15 to 20 values of  $n_{||0}$  are sufficient). The radius  $r_{abs}(n_{||0})$  at which each partial wave is absorbed is thereby evaluated; waves suffering reflection at the confluence with the fast wave (lack of accessibility) or for which the plasma is transparent are disregarded. The values of  $n_{||0}$  corresponding to the transition between reflection and absorption, or to the transition between absorption by the ions and absorption by the electrons, are more accurately determined by successive dicotomy of the corresponding  $n_{||0}$  intervals.

We note that to integrate the ray equations it is necessary to interpolate the profiles, which are known from the transport code only at the mesh points  $r_j$ . This is done with cubic splines, with continuous first and second derivatives. Very smooth interpolation is necessary for the integrating subroutine (a predictor-corrector subroutine kindly made available by O. de Barbieri and D. Jouvet) to achieve the required accuracy.

The function  $r_{Abs}(n_{||a})$  thus obtained for discrete values of  $n_{||a}$  is now in turn interpolated so that it can be inverted to give  $n_{||a}(r_{Abs})$  i.e. the value of the initial parallel index,  $n_{||a}$ , for which the absorption occurs at a given radius  $r_{Abs}$ .

If  $r_j$  is a point of the radial mesh, let  $n_{||j}^+ = n_{||a}(r_j + \frac{\Delta r}{2})$  be the values of  $n_{||a}$  for which absorption occurs at  $r_j \pm \Delta r/2$ , where  $\Delta r$  is the radial step. The power coupled by the antenna in the range  $n_{||j}^- \leq n_{||j} \leq n_{||j}^+$  is attributed to the mesh point  $r_j$ : the power absorbed per unit volume at this radius is thus identified with

$$Q^{LH}(r_j) = \int_{n_{||j}^-}^{n_{||j}^+} P(n_{||}) dn_{||} / (2\pi^2 R r \Delta r) \quad (20)$$

Whether this power has to be attributed to the ions or to the electrons is also immediately clear from the results of ray tracing. The tub heat sources  $Q_i^{LH}(r_j)$  and  $Q_e^{LH}(r_j)$  are now ready for use in the next time step of the tokamak transport code.

## 6. Application to the ASDEX LH-Heating experiment.

The LH heating experiment planned on the ASDEX Tokamak has been described elsewhere /17/.  $V_p$  to 2.4 MW at  $f = 1.3$  GHz will be applied through a Grill consisting of 8 waveguides, each with small side dimension  $b = 3$  cm, and wall thickness  $d = 0.6$  cm. The  $n_{||}$ -spectrum excited by this antenna is



shown in Fig. 1. About 70 % of the power is radiated in the main peak,  $2.3 \lesssim n_{\parallel} \lesssim 4.0$  if the remaining power, two third (20 % of the total) is radiated on harmonics of the main peak (mostly in the third harmonic, peaked around  $n_{\parallel a} \simeq 10$ , not shown in the figure; this power has been disregarded in the computations, as it contributes at most some surface heating); and one third (10 % of the total) in the range  $n_{\parallel} \lesssim 2.3$  in which accessibility problems can arise.

Fig. 2 shows the normalized profiles of density, temperatures and safety factor  $q$ . These profiles were chosen to simulate closely those predicted by a 1-dim. transport code [18], fitted in turn to experimental results from ASDEX.

The safety factor  $q$  at the plasma edge was taken to be 4, corresponding to a current of 250 kA for a plasma radius  $a = 40$  cm, and a toroidal magnetic field  $B_0 = 2.5$  T on the magnetic axis. The central temperatures for ions and electrons were kept fixed,  $T_{i0} = 0.5$  keV and  $T_{e0} = 0.6$  keV, with roughly parabolic profiles. The central density has been varied in the range  $5 \cdot 10^{13} \leq n_0 \leq 1.5 \cdot 10^{14}$ ; the average density is only about 1/6 of these values, since the density is almost linearly decreasing with increasing radius. In this way, we have simulated the typical conditions expected at the beginning of the heating pulse. We have not tried to investigate the situation during the heating, since the effect of heating on the profiles will only be obtained when the ray tracing code will be coupled to the transport code. This work is now in progress.

Fig. 3 shows the radius of maximum penetration (reflection or absorption) as a function of the parallel index at the antenna,  $n_{\parallel a}$ , for three values of the density, in a pure hydrogen plasma. From this figure it is clear that at the lower density,  $n_0 = 6 \cdot 10^{13}$ , only about half of the power in the main peak is absorbed, the plasma being transparent to waves with  $n_{\parallel a} \lesssim 3$ . Full absorption of the main peak occurs at  $n_0 = 8 \cdot 10^{13}$ , and the absorption region is already shifted somewhat to the outside at  $n_0 = 10^{14}$ .

Fig. 4 and 5 show the power deposition profiles  $Q_i(r)$  (in Watt/cm<sup>3</sup> per MW launched by the antenna) for  $n_0 = 6 \cdot 10^{13}$  and  $n_0 = 8 \cdot 10^{13}$  respectively: the efficiency of the absorption is about 45 % in the first case and 70 % in the second case. The latter value is close to the maximum which can be expected, since waves with  $n_{\parallel} \geq 5$  are disregarded in the computation, and waves with  $n_{\parallel} \lesssim 2$  are reflected at low density because of lack of accessibility.

Figs. 6 to 8 show some details of ray tracing for the latter situation,  $n_0 = 8 \cdot 10^{13}$  in pure hydrogen. The ray trajectories in the poloidal cross-section are shown in fig. 6 (the trajectories for negative  $n_{||}$  are just the specular image of these with respect to the equatorial plane). In fig. 7  $n_{||}$  is plotted versus the poloidal angle  $\vartheta$ , showing the characteristic sinusoidal oscillations with minima close to  $\vartheta = \pi$ , which are responsible for the somewhat more severe conditions for accessibility as compared with the slab approximation / 6 /. In Fig. 8  $n_{\perp}$  is plotted versus radius. Here  $n_{||a} = 1.75$  shows the characteristic behaviour of a confluence between the slow and fast wave, while for  $n_{||a} \geq 2.25$  linear transformation into an electrostatic hot plasma wave propagating outwardly with rapidly increasing index is easily recognized.

It is possible to enlarge the range of densities in which absorption by the ions is optimized by slightly modifying the plasma composition. Figs. 9 and 10 show radial penetration versus  $n_{||a}$  and the power deposition profiles  $Q_i(r)$  at  $n_0 = 8 \cdot 10^{13}$  for a few values of the deuterium concentration  $\alpha_D$ . Fig. 11 and 12 are similar, for  $n_0 = 10^{14}$ . From these figure, it is clear that  $\alpha_D$  should not exceed about 0.25. Indeed, increasing  $\alpha_D$  shifts the linear turning point to the inside, but at the same time increases the minimum value of  $n_{||a}$  necessary for accessibility. When this value exceed about 2.5, a non negligible fraction of the power radiated in the main peak cannot reach the centre.

The results of this investigation are summarized in Fig. 13, in which the efficiency of absorption,  $\eta_H$ , is plotted versus the central density for a few values of  $\alpha_D$ .  $\eta_H$  is negligible (within the present model) at low density, and increases sharply as the density exceeds a certain threshold (which is higher the largest the deuterium concentration  $\alpha_D$ ), to reach rapidly the best possible value  $\eta_H \approx 0.7$ . However, if  $\alpha \gtrsim 0.25$  the value of the maximum efficiency decreases because of the just mentioned accessibility problem.

If the density is too large, the heating efficiency will be degraded because the heating region shifts too much towards the edge. A reasonable assumption is to define as high-grade heating contributing to  $\eta_H$  only the power deposited within two third of the plasma radius, i.e. for  $r \leq 26.5$  cm in the present case. With this definition,  $\eta_H$  decreases again sharply at densities above a second threshold, as shown by the dotted curves in Fig.13. The rather sharp definition of the density range in which efficient ion heating occurs is familiar to most LH heating experiments.

## References

- /1/ J.L. Kulp, G.L. Johnston, A. Bers, PRR report 76/9, MIT January 1976
- /2/ K. Ohkubo, K. Ohasa, K. Matsuura, J. Phys. Soc. Japan 43, 642, 1977
- /3/ P.L. Colestock, Nucl. Fusion 18, 740, 1978
- /4/ Yu. F. Baranov, V.I. Fedorov, Sov. Phys. Techn. Phys. Lett. 4, 322, 1978
- /5/ T. Maekawa, Y. Terumichi, S. Tanaka, J. Phys. Soc. Japan 48, 965, 1978
- /6/ Yu. Baranov, V.I. Fedorov, Nucl. Fusion 20, 1111, 1980
- /7/ D.W. Ignat, PPPL-1701, Princeton, Sept. 1980
- /8/ R. Englade et al., 2nd Varenna-Grenoble Int. Symp. On Heating in Toroidal Plasmas, Como 1980, to be published
- /9/ A. Cardinali, M. Brambilla, 2nd Varenna-Grenoble Int. Symp. on Heating of Toroidal Plasmas, Como 1980, to be published
- /10/ M. Brambilla, 2nd Varenna-Grenoble Int. Symp. on Heating in Toroidal Plasmas, Como 1980, to be published
- /11/ V.E. Golant, Sov. Phys. Techn. Phys. 16, 1980, 1972
- /12/ T.H. Stix, Phys. Rev. Lett. 15, 878, 1965
- /13/ M. Brambilla, A. Cardinali, to be published
- /14/ CFF Karney, Phys. Fluids 22, 2188, 1979
- /15/ M. Brambilla, Nucl. Fusion 18, 493, 1978
- /16/ M. Brambilla, Nucl. Fusion 16, 47, 1976
- /17/ H. Brinkschulte et al., 2nd Varenna-Grenoble Int. Symp. on Heating in Toroidal Plasmas, Como 1980, to be published
- /18/ D. Eckhardt, A. McKenney, Transport Code Predictions on the Performance of Lower Hybrid Heating in the ASDEX Tokamak, IPP-Report 4/197, Garching, March 1981



Figure captions

- Fig. 1: Power spectrum excited by the ASDEX Grill
- Fig. 2: Normalized profiles for  $n(r)$ ,  $T_i(r)$ ,  $T_e(r)$  and  $q(r)$
- Fig. 3: Radius of maximum penetration versus  $n_{||a}$ .  
Pure hydrogen plasma.
- Fig. 4: Power deposition profile, pure Hydrogen plasma,  
 $n_0 = 6 \cdot 10^{13}$ .
- Fig. 5: Power deposition profile, pure Hydrogen plasma,  
 $n_0 = 8 \cdot 10^{13}$ .
- Fig. 6: Ray trajectories for sampled  $n_{||a}$  values in the  
poloidal cross-section. Pure Hydrogen plasma,  $n_0 = 8 \cdot 10^{13}$ .
- Fig. 7:  $n_{||}$  versus poloidal angle. Same plasma as Fig. 6
- Fig. 8:  $n_{\perp}$  versus radius. Same plasma as Fig. 6
- Fig. 9: Radius of maximum penetration versus  $n_{||a}$  at  $n_0 = 8 \cdot 10^{13}$ ,  
varying the deuterium concentration.
- Fig. 10: Power deposition profiles for the cases of Fig. 9.
- Fig. 11: Radius of maximum penetration versus  $n_{||a}$ , at  $n_0 = 10^{14}$ ,  
varying the deuterium concentration.
- Fig. 12: Power deposition profiles for the cases of Fig. 11.
- Fig. 13: Heating efficiency versus density, varying the  
deuterium concentration.

fig.1

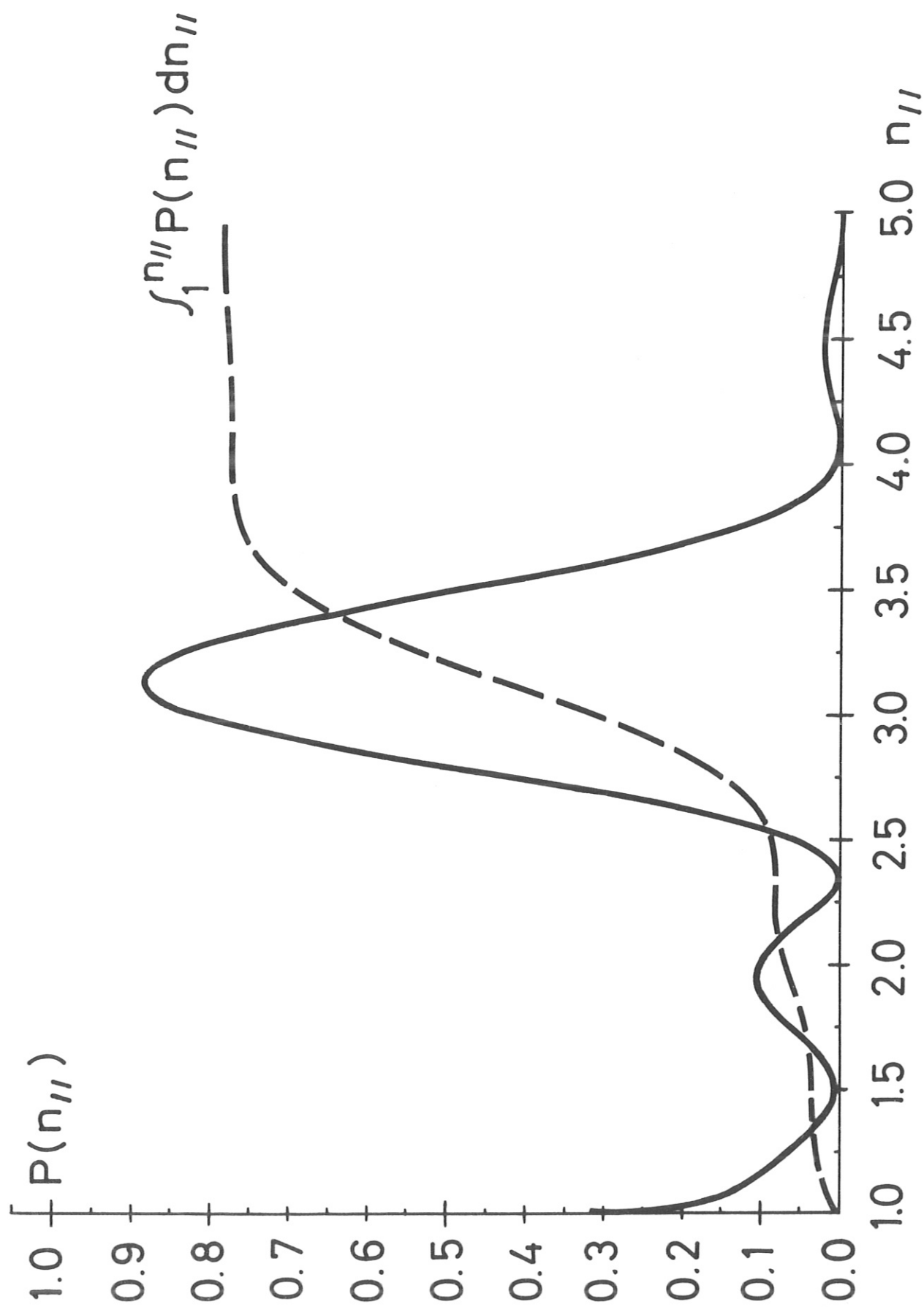


fig.2

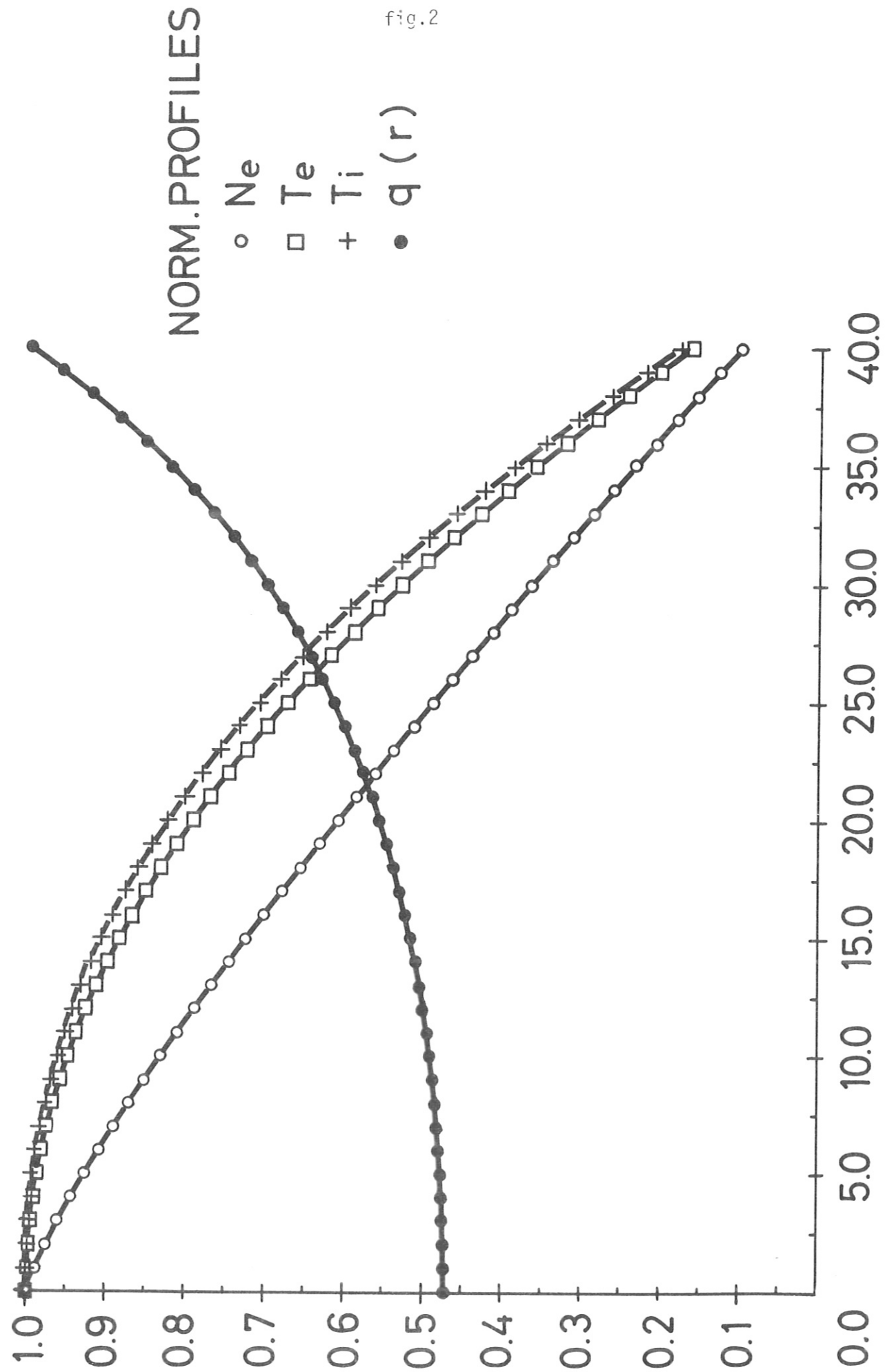




fig.3

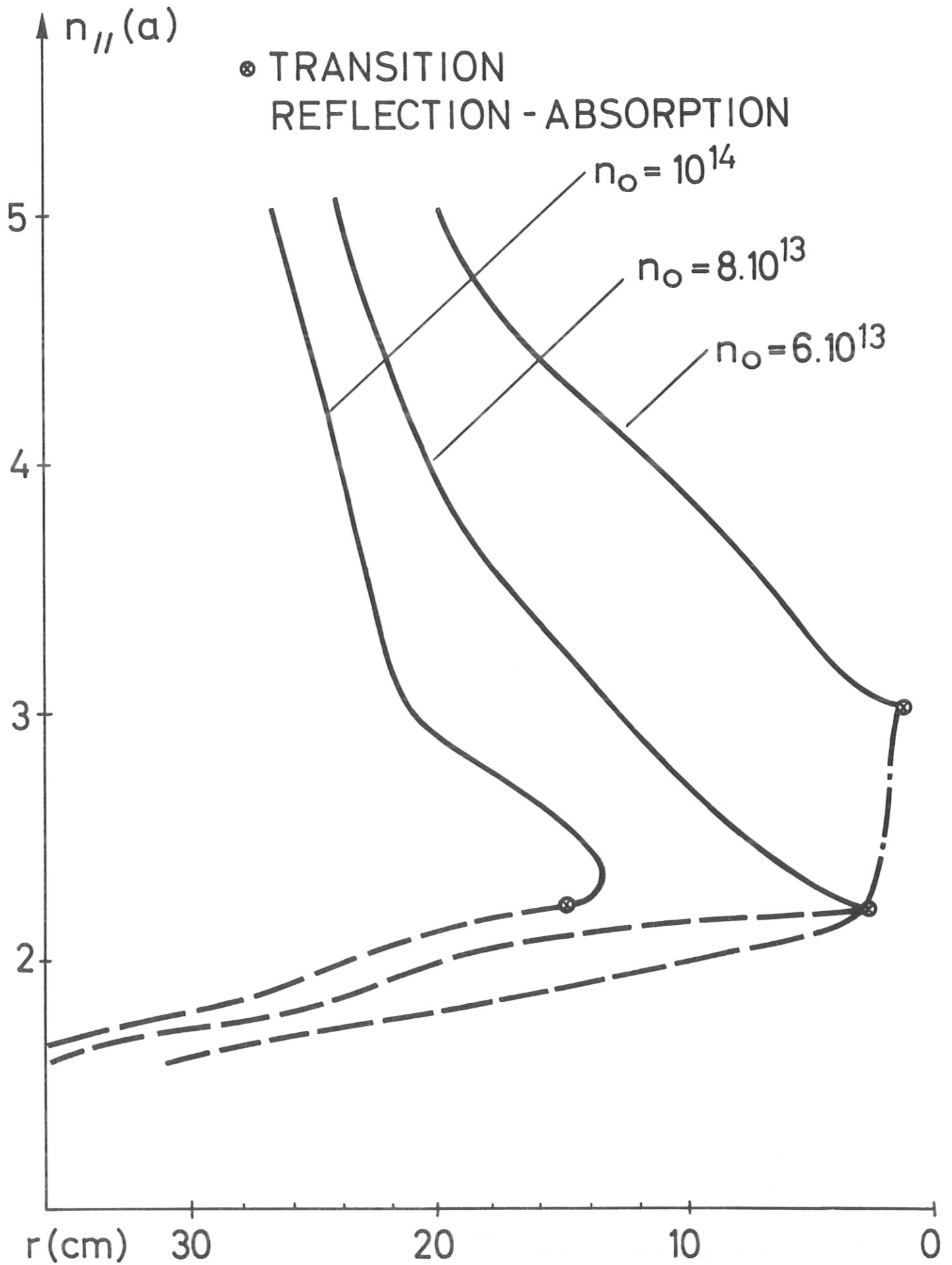


fig.4

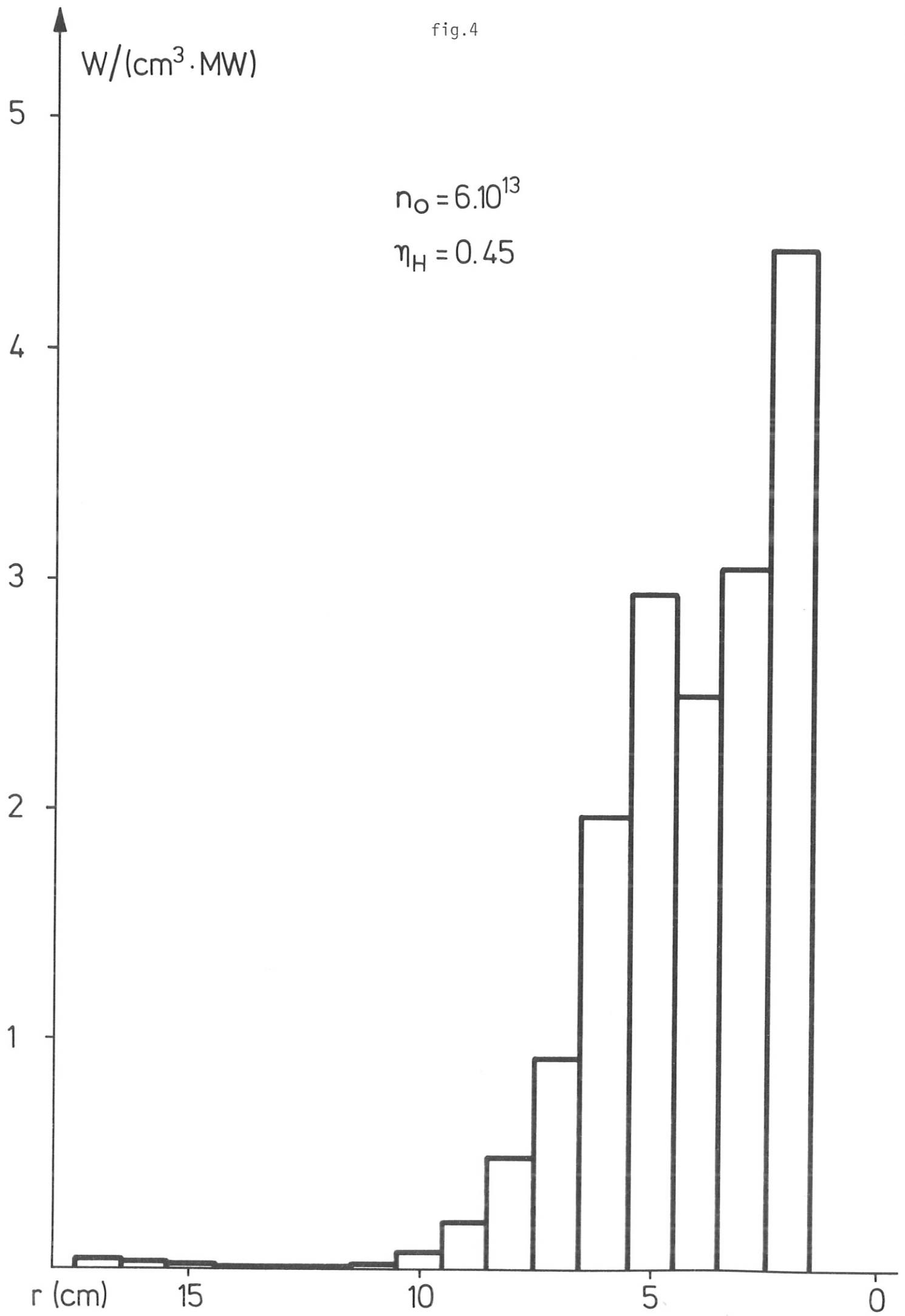


fig.5

$W/(\text{cm}^3 \cdot \text{MW})$

$$n_o = 8 \cdot 10^{13}$$

$$\eta_H = 0.70$$

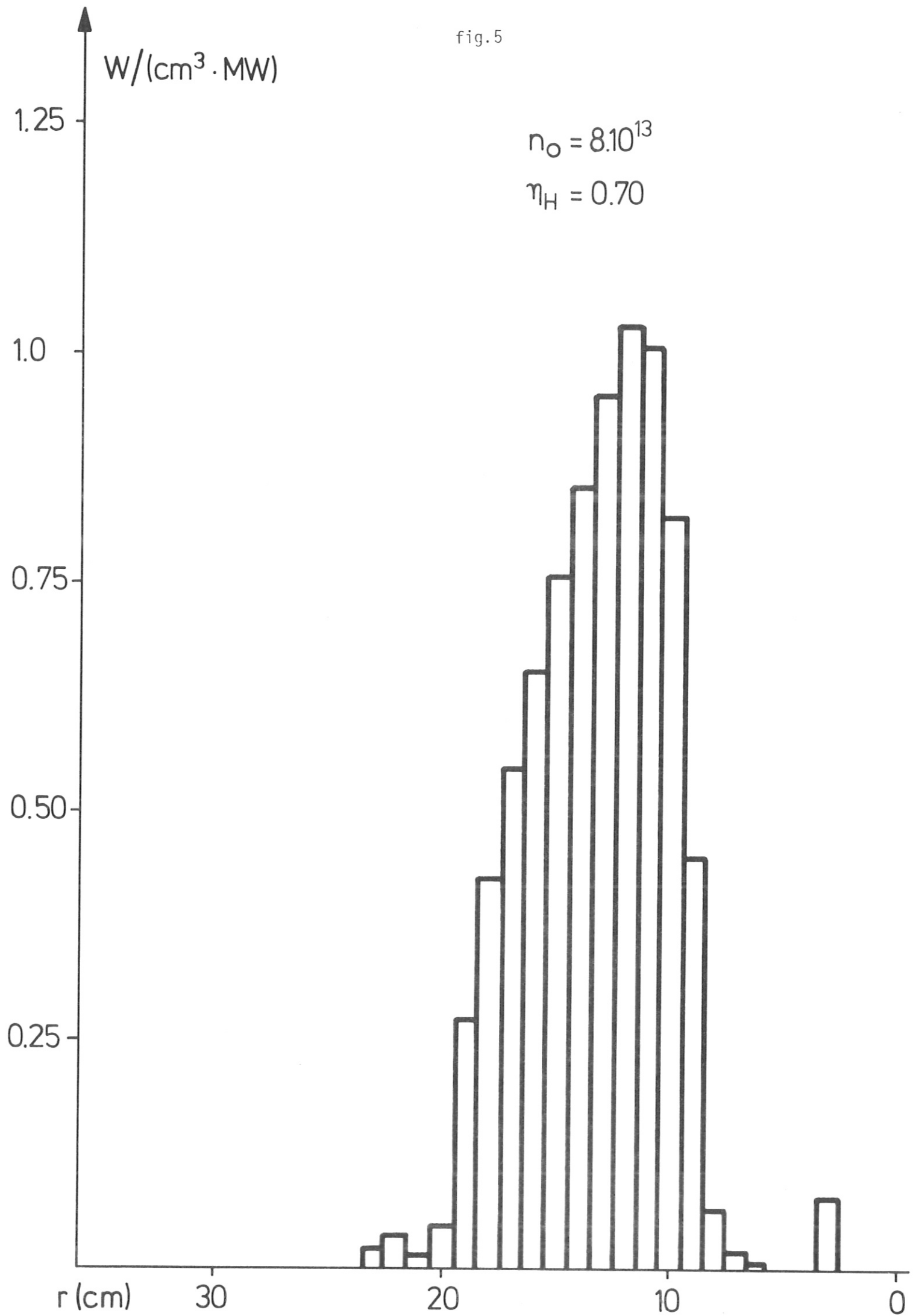


fig.6

$$n_0 = 0.80 \cdot 10^{14} \text{ cm}^{-3}$$

$$T_{i0} = 0.50 \text{ Kev}$$

$$T_{e0} = 0.60 \text{ Kev}$$

$$q(a) = 4.00$$

$$N_{\prime\prime}(a) = 1.75$$

$$2.25$$

$$2.75$$

$$3.25$$

$$3.75$$

$$4.25$$

$$4.75$$

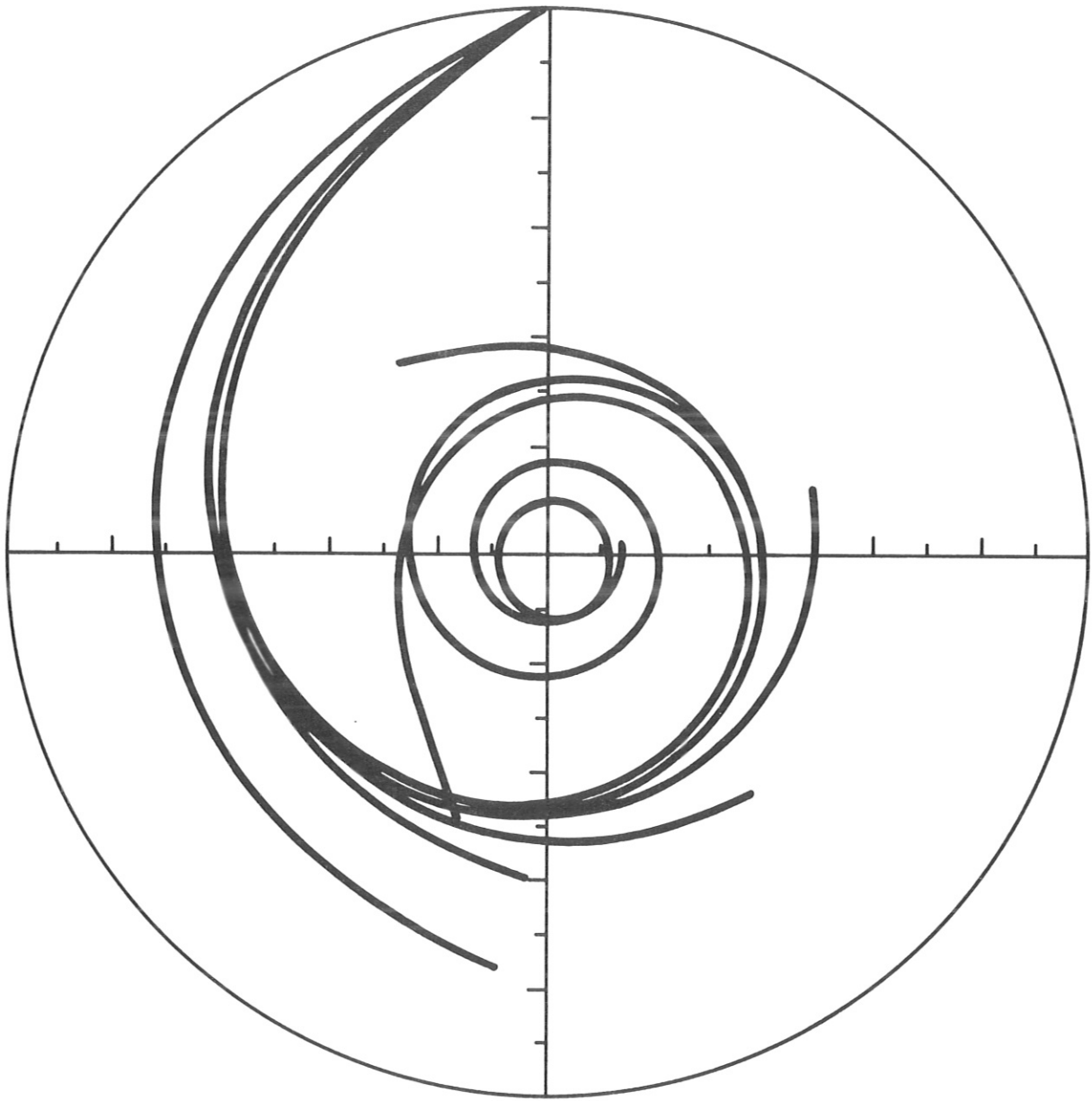


fig.7

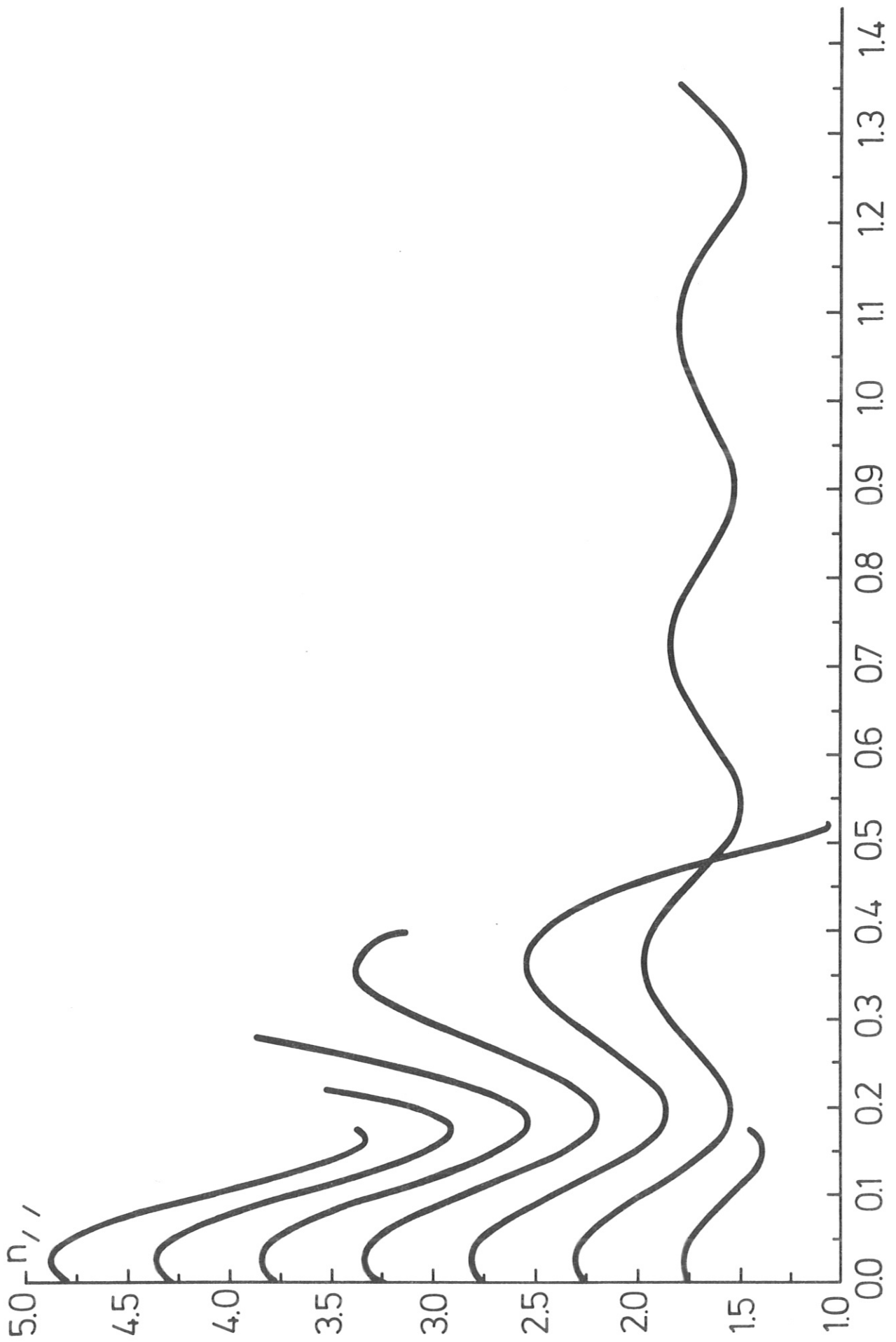




fig. 8

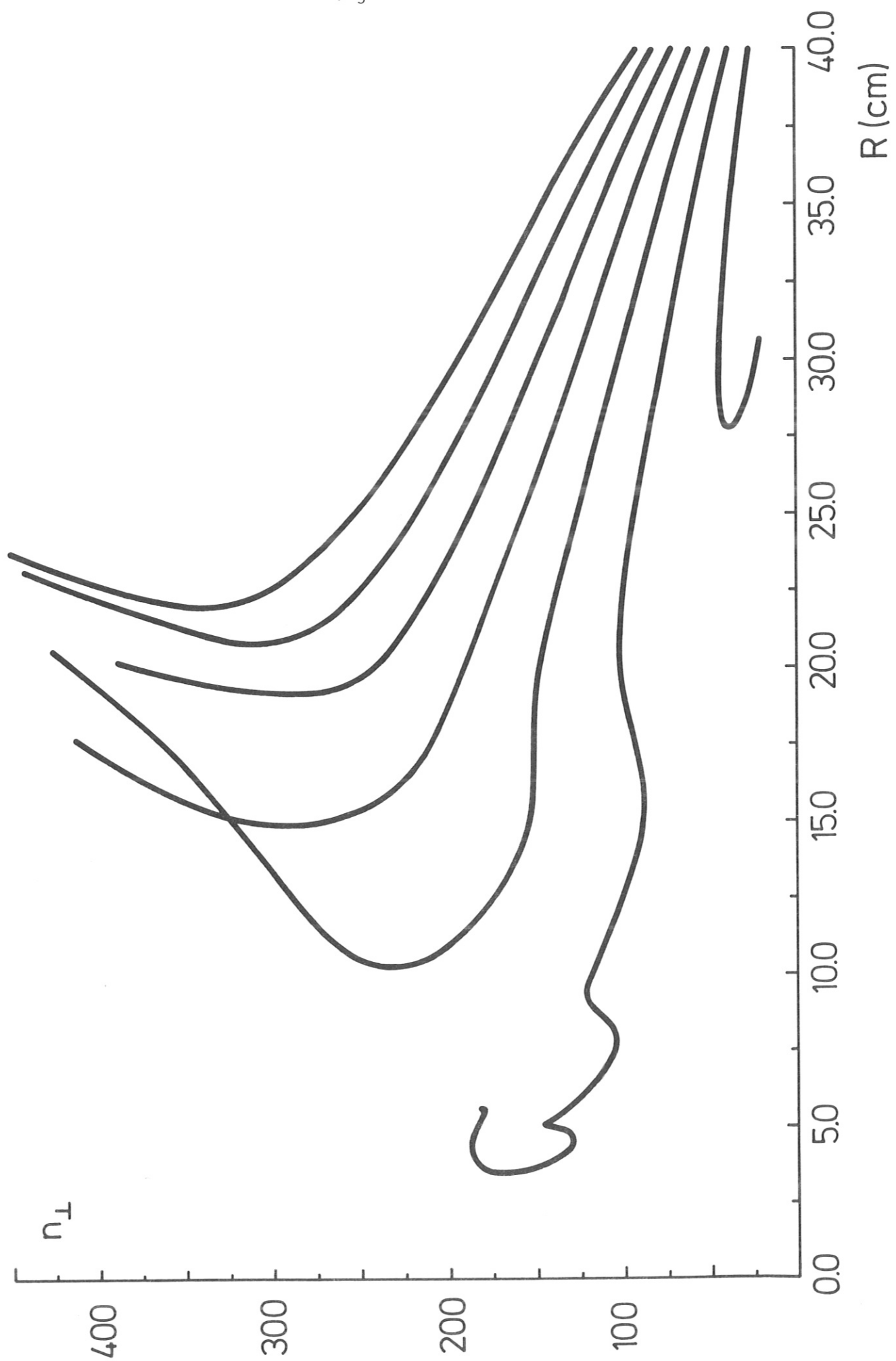


fig.9

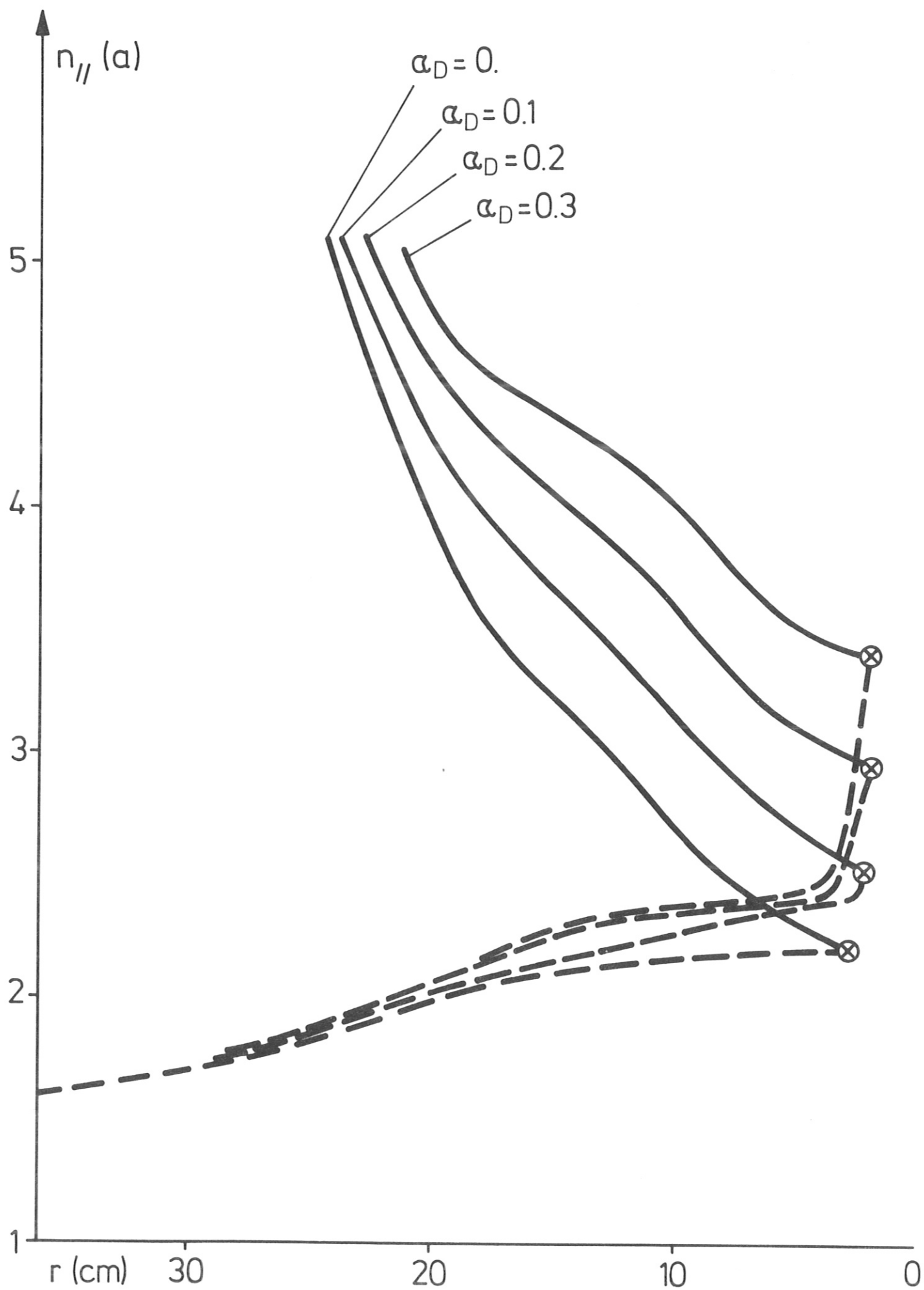


fig.10

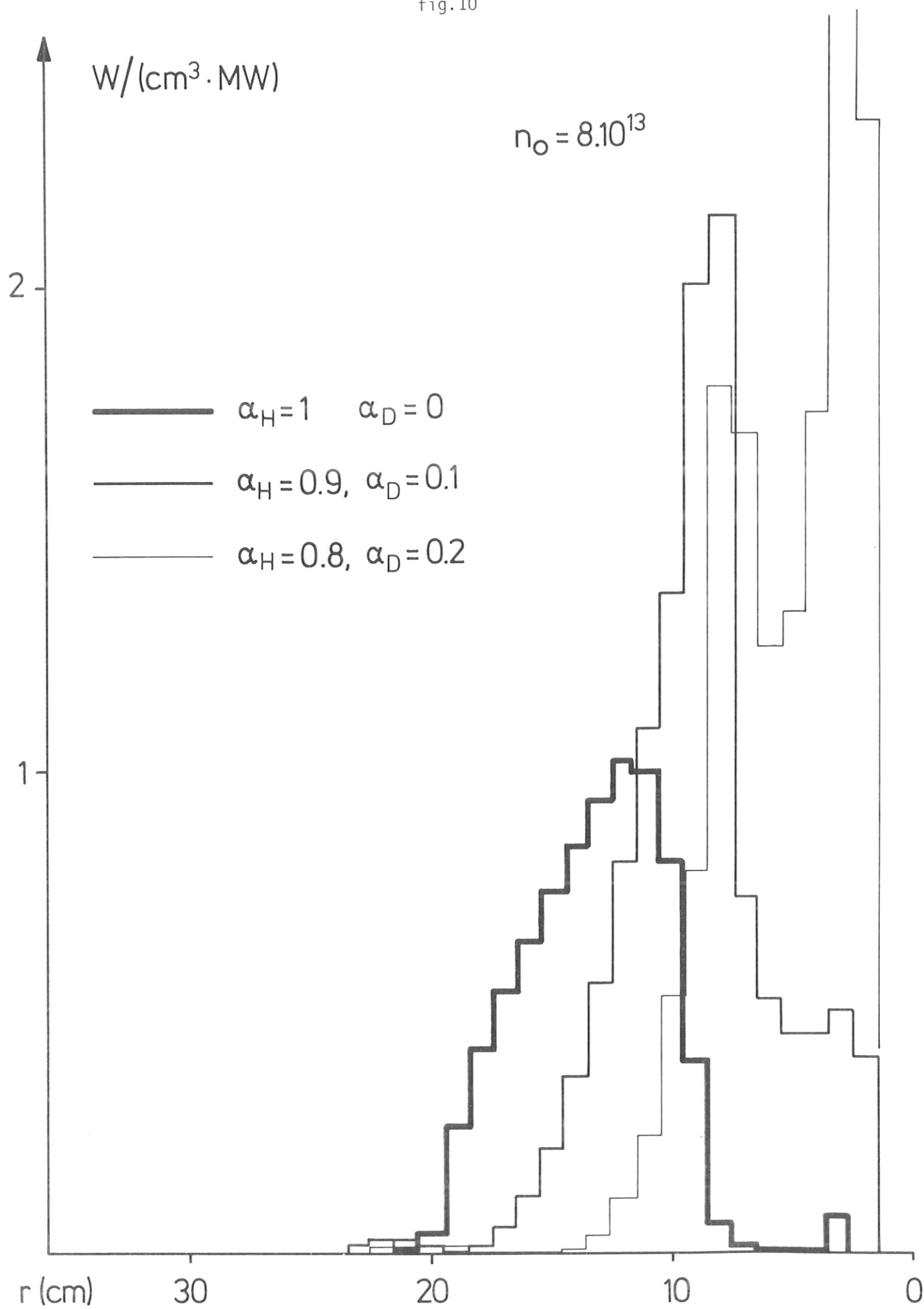


fig.11

$$n_0 = 10^{14}$$

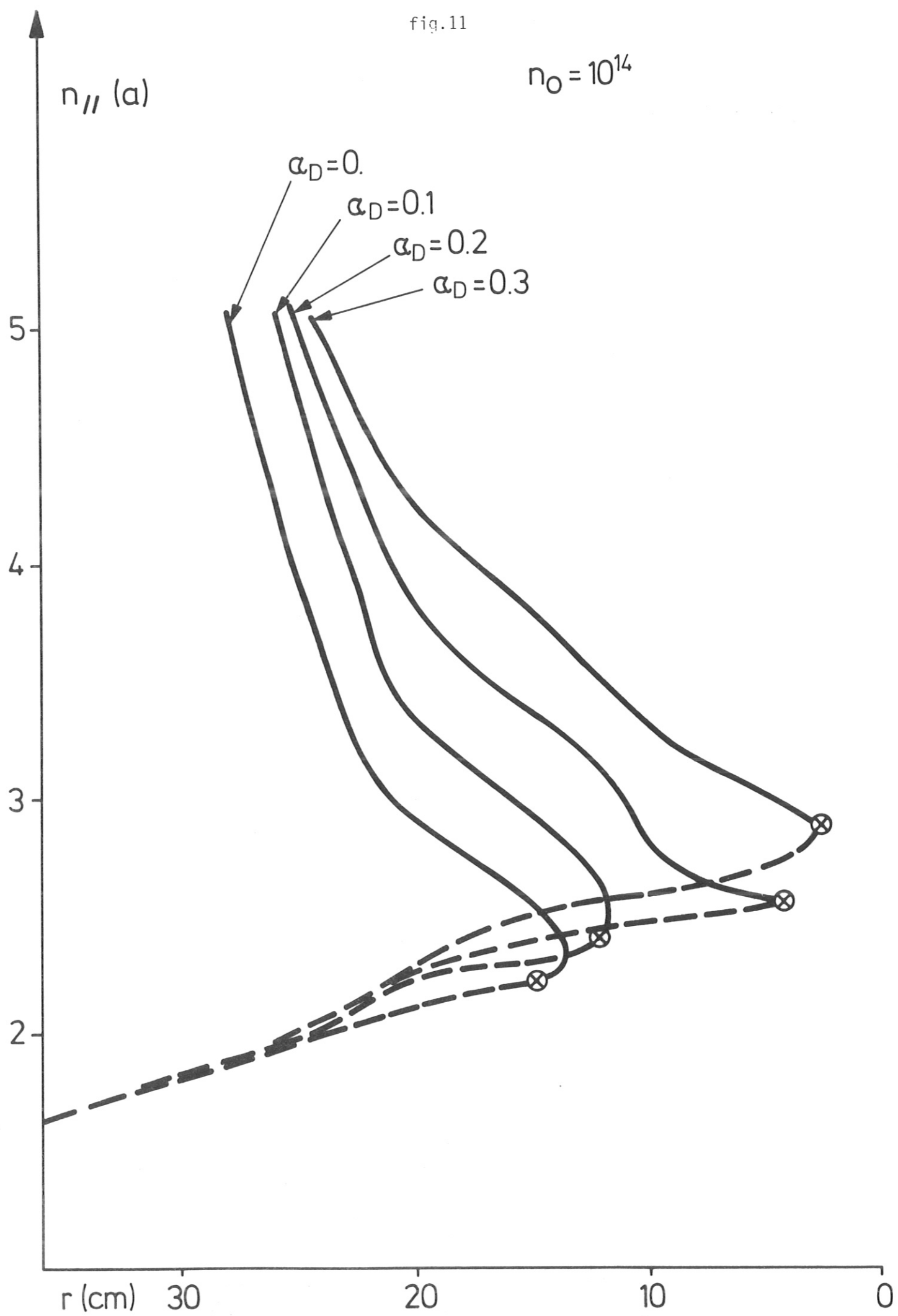


fig.12

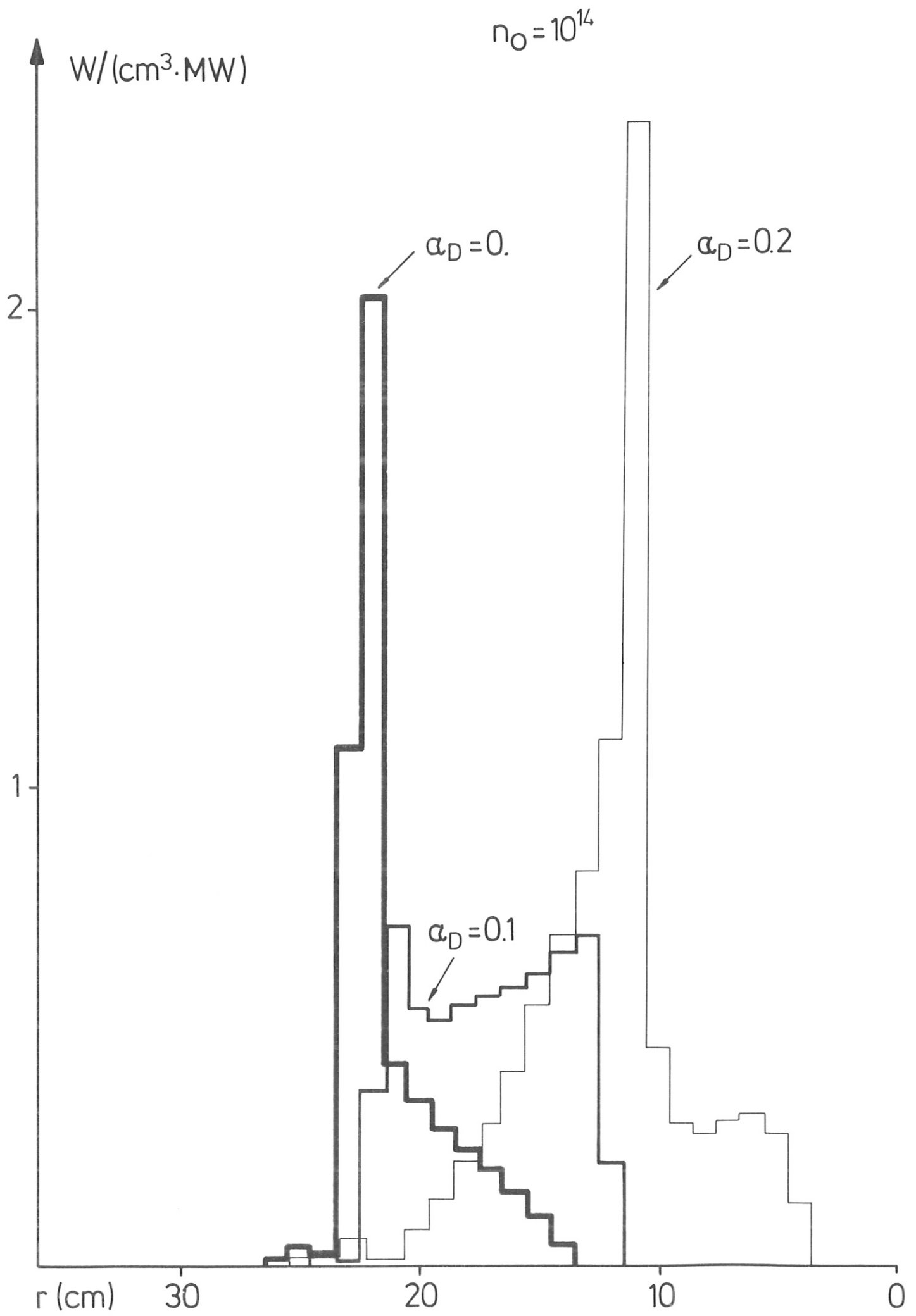




fig.13

